Wavelet-based adaptive unsteady Reynolds-averaged Navier-Stokes computations of wall-bounded internal and external compressible turbulent flows

Xuan Ge*[1], Oleg V. Vasilyev†[2,3,4], Giuliano De Stefano‡[5], and M. Yousuff Hussaini§[1]

[1] *Florida State University, Tallahassee, FL 32306, USA*
[2] *Skolkovo Institute of Science and Technology, Moscow 143026, Russia*
[3] *NorthWest Research Associates, Boulder CO 80301, USA*
[4] *University of Colorado, Boulder CO 80309, USA*
[5] *Università della Campania, Aversa I-81031, Italy*

The Wavelet-based Unsteady Reynolds-Averaged Navier-Stokes (W-URANS) turbulence modeling approach is proposed for simulations of wall-bounded internal and external compressible turbulent flows. The new approach utilizes anisotropic wavelet-based mesh refinement and its effectiveness is demonstrated in the case of flow simulations with two turbulence models, namely the $k-\omega$ and Spalart-Allmaras models. Supersonic plane channel flow and weakly compressible channel flow with periodic hill constrictions are tested as internal benchmark flows, while a flow past a circular cylinder at sub-critical Reynolds number is used as a prototype for an external flow. The effectiveness of the W-URANS approach is demonstrated for a number of two- and three-dimensional benchmark problems by comparing the results of the W-URANS simulations with results already available in the literature. It has been observed that the three-dimensional simulations for separated flows are able to capture the 3D vortical structures, which can thereby improve the RANS performance compared to conventional non-adaptive low-resolution unsteady RANS methods. The current study serves as a baseline for the development of a unified hierarchical eddy resolving turbulence modeling framework, capable of performing simulations of different fidelities: from non-modeling direct numerical simulations to full-modeling RANS simulations.

I. Introduction

In applications of aerodynamics and turbomachinery, numerical simulation is playing an increasingly important role for investigations of turbulent flows, especially in compressible regimes. Unlike incompressible regimes, the fluid dynamics is fairly complicated by significant variations of thermodynamic characteristics in the high Mach number regimes. High fidelity methods, *i.e.* direct numerical simulations (DNS), remain computationally prohibitive for moderate and high Reynolds number flows due to the wide range of length and time scales and the resulting computational requirements that exceed current capabilities.

The latest advances in wavelet-based numerical methodologies to solve partial differential equations,[1–5] combined with the unique properties of wavelet analysis to identify and isolate localized dynamically dominant flow structures,[6,7] and to track them on adaptive computational meshes,[8–12] have demonstrated the convenience of spatio-temporal mesh adaptation for numerical simulations of turbulent flows. The wavelet-based methods with inherent adaptive mesh refinement capabilities and sparse data representation not only take full advantage of spatio-temporal intermittency of turbulent flows by substantially reducing the number

*Postdoctoral Scholar, Department of Mathematics, Florida State University
†Professor, Center for Design, Manufacturing and Materials, Skolkovo Institute of Science and Technology; Sr. Research Scientist, NorthWest Research Associates;
Professor, Department of Mechanical Engineering, University of Colorado, AIAA Senior Member
‡Professor, Dipartimento di Ingegneria Industriale e dell'Informazione, Università della Campania
§Professor of Mathematics and Computational Science & Engineering, AIAA Fellow

of degrees of freedom and, consequently, the computational cost, but also provide a systematic framework for active error control.

Further tight integration of adaptive wavelet-based method with turbulence modeling allows the construction of a hierarchical framework for simulating turbulent flows[13] where coherent flow structures are either totally or partially resolved on self-adaptive computational grids, while modeling the effect of unresolved motions. The separation between resolved (more energetic) eddies and residual (less energetic) flow is achieved by means of nonlinear wavelet thresholding filter. The value of wavelet threshold controls the relative importance of resolved field and residual background flow and, thus, the fidelity of turbulence simulations. By increasing the thresholding level, a unified **hierarchy** of wavelet-based turbulence models of different fidelities can be obtained. Wavelet-based direct numerical simulation (WDNS), coherent vortex simulation (CVS)[6] and wavelet-based stochastic coherent adaptive large-eddy simulation (SCALES),[7] also referred to as Adaptive LES, represent different fidelity methods within this hierarchy. A distinct advantage of the adaptive wavelet-based hierarchical framework is that the overall physical fidelity of the simulation can be simply controlled by the adaptive wavelet threshold filter,[14,15] thereby providing a fully unified hierarchical modeling framework that allows transition continuously among various fidelities, from WDNS to CVS to Adaptive LES, and even to W-URANS simulations.

Transition from DNS to CVS to Adaptive LES through controlling wavelet threshold is well established. WDNS uses wavelet-based discretization of the Navier-Stokes equations to adapt dynamically the local resolution of intermittent flow structures.[12,16,17] Transition from WDNS to CVS[6] is achieved by using an optimal wavelet threshold, resulting in the decomposition of the flow field into coherent and non-coherent contributions. For Adaptive LES, the wavelet threshold is further increased so that the stochastic and the least energetic coherent portion of the turbulent solution are discarded and only the most energetic part of the coherent vortices are captured in the resolved field.[7] However, an adaptive hybrid approach with coexistence, connection and even active communication between W-URANS and Adaptive LES regions in a mathematically consistent fashion has not been developed. The present study is the first step toward extending the Hierarchical Eddy Resolving Approach to include W-URANS.

Wavelet-based adaptation, discussed above, employs tensorial wavelets and results in isotropic mesh refinement, which unnecessarily increases the number of degrees of freedom and, thus, the computational cost of high Reynolds number wall-bounded flow simulations, where high gradients of velocity and temperature may occur within the thin boundary layers. The recently developed Adaptive-Anisotropic Wavelet Collocation Method (A-AWCM)[18] addresses this limitation by allowing the use of body-fitted curvilinear meshes while preserving the essential features of the classical wavelet-based adaptation procedure, *i.e.* the error control of the numerical solution and the fully automated mesh refinement.

In addition to A-AWCM, the RANS modeling approach is also a necessity for simulations of high Reynolds number wall-bounded internal and external flows with complex geometries in practical or industrial applications. In this paper a novel Wavelet-based adaptive Unsteady Reynolds-Averaged Navier-Stokes (W-URANS) approach utilizing A-AWCM for numerical computations of compressible unsteady RANS equations is presented. It can handle body-fitted grid for arbitrary geometry and stream-wise periodic boundary condition. Both a two-equation model ($k-\omega$) and a one-equation model (Spalart-Allmaras, S-A) are examined in this work. The W-URANS modeling approach is first demonstrated for 2D supersonic plane channel flow by comparing the friction velocity based Reynolds number Re_τ and the mean profiles with the DNS data available in the literature. Then a channel flow with periodic hill constrictions is presented to demonstrate the capability of W-URANS along with A-AWCM, where the geometry becomes complex and a body-fitted mesh in physical domain is used. Finally, the results for the flow past a circular cylinder, a typical external flow case, are presented for the new W-URANS approach. The results for both 2-D and 3-D simulations are included in this paper for these statistically steady or unsteady flows. It has been observed that unlike conventional URANS simulation, the W-URANS in 3D cases is able to capture the 3D vortical structures and thereby produce substantial improvement with respect to conventional low-resolution non-adaptive URANS.[19]

This paper is organized as follows. Section II introduces the governing equations of the simulations, including the Favre-averaged Navier-Stokes equations for compressible flows and the evolution equations for turbulence models. The wavelet-based adaptive methods and the A-AWCM for complex domain geometries are described in Section III. The simulation environment and corresponding results are presented and discussed in Section IV. Concluding remarks are given at the end in Section V.

II. Governing Equations

II.A. Favre-averaged Navier-Stokes equations

The Favre-averaged Navier-Stokes equations for conservation of mass, momentum, and energy in compressible flows with modeled turbulent terms are written below.

$$\frac{\partial \rho}{\partial t} + \frac{\partial (\rho u_j)}{\partial x_j} = 0, \tag{1}$$

$$\frac{\partial \rho u_i}{\partial t} + \frac{\partial}{\partial x_j}\left(\rho u_i u_j\right) = -\frac{\partial p}{\partial x_i} + \frac{\partial \hat{\tau}_{ij}}{\partial x_j}, \tag{2}$$

$$\frac{\partial \rho e}{\partial t} + \frac{\partial}{\partial x_j}\left[\left(\rho e + p\right) u_j\right] = \frac{\partial}{\partial x_j}\left[u_i \hat{\tau}_{ij} - q_j\right] + \frac{\partial}{\partial x_j}\left[\left(\mu + \sigma^* \frac{\rho k}{\omega}\right)\frac{\partial k}{\partial x_j}\right], \tag{3}$$

where

$$p = \rho R T, \tag{4}$$

$$e = \frac{1}{2} u_i u_i + \frac{p}{\rho(\gamma - 1)} + k, \tag{5}$$

$$\begin{aligned} q_j &= -c_p \left(\frac{\mu}{Pr_L} + \frac{\mu_T}{Pr_T}\right)\frac{\partial T}{\partial x_j}, \\ \hat{\tau}_{ij} &= 2\mu \tilde{S}_{ij} + \tau_{ij}, \\ \tau_{ij} &= 2\mu_T \tilde{S}_{ij} - \frac{2}{3}\rho k \delta_{ij}, \\ \tilde{S}_{ij} &= \mathrm{dev}(S_{ij}) = S_{ij} - \frac{1}{3}\frac{\partial u_k}{\partial x_k}\delta_{ij}, \\ S_{ij} &= \frac{1}{2}\left(\frac{\partial u_i}{\partial x_j} + \frac{\partial u_j}{\partial x_i}\right), \end{aligned} \tag{6}$$

where ρ is the the Reynolds-averaged density of the fluid (gas), p is the Reynolds-averaged pressure, ρu_j is the mass flux, u_j is the Favre-averaged velocity, T is the Favre-averaged temperature, and e is the Favre-averaged total energy per unit mass. Parameter R is the gas constant, while c_v and c_p are the specific heats at constant volume and pressure, respectively. The specific heat ratio $\gamma = \frac{c_p}{c_v} \equiv 1.4$ for diatomic gases, and $Pr = \frac{\mu c_p}{\lambda}$ is the Prandtl number. The term q_j is sum of both the laminar and modeled turbulent heat flux vectors with $Pr_L = 0.72$ and $Pr_T = 0.9$ being the laminar and turbulent Prandtl numbers respectively. The turbulent eddy viscosity is denoted by μ_T, which is unknown and needs turbulence models for closure. The term $\hat{\tau}_{ij}$ is the sum of the molecular and Reynolds stress tensors, while τ_{ij} is the Reynolds stress tensor, S_{ij} is the mean strain-rate tensor, and $\tilde{S}_{ij}$ is the deviatoric tensor of S_{ij}. The temperature dependent dynamic molecular viscosity μ is given by the Sutherland's law,

$$\frac{\mu}{\mu_{ref}} = \frac{T_{ref} + S}{T + S}\left(\frac{T}{T_{ref}}\right)^{3/2}, \tag{7}$$

where the constants $S = 110.4K$ and $T_{ref} = 293.15K$.

The highlighted terms in Eq. (3), (5) and (6) are retained only for the $k-\omega$ model and are neglected for the Spalart-Allmaras model.

II.B. Turbulence model equations

Two RANS models are considered in this paper : the $k-\omega$ model and the Spalart-Allmaras model. Both models use auxiliary transport equations with the Favre-averaged Navier-Stokes equations to solve turbulence quantities, such as turbulent kinetic energy k, specific turbulent dissipation rate ω, and effective viscosity $\tilde{\mu}$ tightly associated with the eddy viscosity μ_T, which is modeled as a function of these turbulence quantities. Therefore the closure terms with μ_T in the mean flow equations can be evaluated.

Note that in contrast to conventional RANS methods, where the grid is specified *a priori*, our approach uses a dynamically adaptive grid. The finest grid resolution scales allowed in our adaptive W-URANS method

could be considerably smaller than the commonly accepted ones in conventional non-adaptive RANS method due to the presence of dynamically evolved small scale structures. These small structures may not be damped by model dissipation and need to be resolved in the W-URANS simulations. Note that these small-scale structures are not typically supported by non-adaptive RANS meshes.

Conventional RANS computations use dissipative numerical schemes to damp small scale 3D vortical structures and to resolve only smooth quasi one-dimensional eddies. When the same simulations are done using adaptive methods with finer resolution and higher order non-dissipative schemes like the ones used in this work, larger eddies cascade into less energetic smaller scales structures, which should be captured by the adaptive mesh. Our numerical experiments shows that well-resolved solution near the wall results in fewer adaptive grid points. If the localized eddies are not properly resolved, aliasing errors may arise and spread into wider regions resulting in more grid points.

It is known that the widely used $k-\varepsilon$ model needs a near-wall treatment using either wall functions or damping functions in the viscous sublayer due to the over-prediction of the eddy viscosity in the law-of-the-wall layer (between $y^+ = 0$ *to* 40). When a wall function is used, the first wall neighboring grid point must reside in the log-layer and hence it cannot be readily accommodated in the adaptive wavelet method mentioned above where the near-wall resolution should be $y^+ \sim O(0.1)$. At the same time, the $k-\omega$ model[20] without any wall functions or near-wall damping functions has been shown to be usable because of its underestimation of the turbulent kinetic energy k and overestimation of the dissipation rate ε near the wall.[21] These two features are exactly what are needed to counter overestimation of μ_T in the $k-\varepsilon$ model. Since the $k-\omega$ model is constantly undergoing revision and improvement, a recent version of the model proposed by Wilcox (2008)[22] with zero round-jet parameter χ_ω is selected in this paper. The two evolution equations are written as

$$\frac{\partial \rho k}{\partial t} + \frac{\partial}{\partial x_j}(\rho k u_j) = \tau_{ij}\frac{\partial u_i}{\partial x_j} + \frac{\partial}{\partial x_j}\left[(\mu + \sigma^*\frac{\rho k}{\omega})\frac{\partial k}{\partial x_j}\right] - \rho\beta^* k\omega, \tag{8}$$

$$\frac{\partial \rho \omega}{\partial t} + \frac{\partial}{\partial x_j}(\rho \omega u_j) = \alpha\frac{\omega}{k}\tau_{ij}\frac{\partial u_i}{\partial x_j} + \frac{\partial}{\partial x_j}\left[(\mu + \sigma\frac{\rho k}{\omega})\frac{\partial \omega}{\partial x_j}\right] - \rho\beta\omega^2 + \sigma_{d0}\frac{\rho}{\omega}\max(0, \frac{\partial k}{\partial x_j}\frac{\partial \omega}{\partial x_j}), \tag{9}$$

where

$$\mu_T = \rho k/\tilde{\omega},,$$
$$\tilde{\omega} = \max\left(\omega, C_{\lim}\sqrt{\frac{2\tilde{S}_{ij}\tilde{S}_{ij}}{\beta^*}}\right),$$

k is the turbulent kinetic energy, ω is the specific dissipation rate. The constant coefficient $C_{\lim} = 7/8$, $\alpha = 5/9$, $\beta^* = 9/100$, $\beta = 0.0708$, $\sigma = 1/2$, $\sigma_d = 1/8$ and $\sigma^* = 3/5$.

On the solid wall, the velocity must satisfy the no-slip conditions, while temperature, turbulent kinetic energy, and specific dissipation rate of the obstacles are assumed constant,

$$\left.\begin{array}{l} \mathbf{u} = 0 \\ T = T_w \\ k = 0 \\ \omega = \omega_w = \frac{C\mu}{\rho(\delta_h)^2} \end{array}\right\} \text{ on } \partial O_i,\ \forall i, \tag{10}$$

where T_w is the temperature of the solid wall, and constant $C = 80$ is chosen to set the required resolution δ_h, depending on the first neighboring grid spacing normal to the wall.

The two-equation model described above results in an eddy viscosity from turbulence velocity ($\sqrt{k}$) and time ($1/\omega$) scales. Spalart and Allmaras[23] proposed a transport equation directly for the eddy viscosity. The Spalart-Allmaras model has enjoyed great success in predicting aerodynamic flows,[24] especially for high Mach flows, where the compressibility effect cannot be neglected. The standard Spalart-Allmaras model[23] in terms of $\rho\tilde{\nu}$ is written as

$$\begin{aligned}\frac{\partial \rho\tilde{\nu}}{\partial t} + \frac{\partial}{\partial x_j}(\rho\tilde{\nu}u_j) &= c_{b1}(1-f_{t2})\tilde{S}\rho\tilde{\nu} - \left[c_{w1}f_w - \frac{c_{b1}}{\kappa^2}f_{t2}\right]\rho\left(\frac{\tilde{\nu}}{d}\right)^2 \\ &+ \frac{\partial}{\partial x_j}\left[\left(\frac{\mu}{\sigma} + \frac{\rho\tilde{\nu}}{\sigma}\right)\frac{\partial\tilde{\nu}}{\partial x_j}\right] - \left(\frac{\mu}{\sigma\rho} + \frac{\tilde{\nu}}{\sigma}\right)\frac{\partial\rho}{\partial x_j}\frac{\partial\tilde{\nu}}{\partial x_j} + c_{b2}\frac{\rho}{\sigma}\frac{\partial\tilde{\nu}}{\partial x_j}\frac{\partial\tilde{\nu}}{\partial x_j},\end{aligned} \tag{11}$$

and the eddy viscosity is computed from:

$$\mu_T = \rho\tilde{\nu} f_{v1}, \tag{12}$$

where

$$\begin{aligned}
f_{v1} &= \frac{\chi^3}{\chi^3 + c_{v1}^3}, \\
\chi &= \tilde{\nu}/\nu, \\
\tilde{S} &= \max\left[0.3\sqrt{2\Omega_{ij}\Omega_{ij}}, \sqrt{2\Omega_{ij}\Omega_{ij}} + \frac{\tilde{\nu}}{\kappa^2 d^2} f_{v2}\right], \\
\Omega_{ij} &= \frac{1}{2}\left(\frac{\partial u_i}{\partial x_j} - \frac{\partial u_j}{\partial x_i}\right), \\
f_{v2} &= 1 - \frac{\chi}{1 + \chi f_{v1}}, \\
f_w &= g\left[\frac{1 + c_{w3}^6}{g^6 + c_{w3}^6}\right]^{1/6}, \\
g &= r + c_{w2}(r^6 - r), \\
r &= \min\left[\frac{\tilde{\nu}}{\tilde{S}\kappa^2 d^2}, 10\right], \\
f_{t2} &= c_{t3}\exp(-c_{t4}\chi^2),
\end{aligned}$$

and d is the distance from the field point to the nearest wall. To avoid possible numerical problems, Spalart (private communication) suggests limiting $\tilde{S}$ to be no smaller than $0.3\sqrt{2\Omega_{ij}\Omega_{ij}}$. $c_{b1} = 0.1355$, $c_{b2} = 0.622$, $\sigma = 2/3$, $\kappa = 0.41$, $c_{w2} = 0.3$, $c_{w3} = 2$, $c_{v1} = 7.1$, $c_{w1} = \frac{c_{b1}}{\kappa} + \frac{1+c_{b2}}{\sigma}$. This "standard" version of the S-A model does not have the trip term "f_{t1}", and hence it is argued that f_{t2} is not necessary, i.e. $c_{t3} = 0$. The no-slip wall boundary condition for $\tilde{\nu}$ is $\tilde{\nu} = 0$.

III. Wavelet-based Adaptive Computations

The turbulence models described above are implemented using the parallel Adaptive Wavelet Collocation method (AWCM).[5] The unsteady RANS governing equations are evaluated at collocation points, which are adapted in space and time to dynamically resolve all the features of the numerical solution. The essential features of the AWCM are briefly described in the next two sections. For detailed discussion the reader is referred to Refs. 1, 2, 5, 18. A novel treatment of periodic boundary conditions is described in Section III.C.

III.A. Adaptive Wavelet Collocation Method

The Adaptive Wavelet Collocation Method is based on multi-resolution wavelet analysis to construct time-dependent computational meshes with spatially varying resolution, required to adequately resolve the localized features of the solution with *a priori* prescribed accuracy. The grid adaptation is based on the analysis of wavelet decomposition of a spatially dependent field, say $u(\mathbf{x})$, sampled on a set of dyadic nested collocation points $\mathbf{x}_\mathbf{k}^j$ at different levels of resolution j, formally written as

$$u(\mathbf{x}) = \sum_{\mathbf{l}\in\mathcal{L}^1} c_\mathbf{l}^1 \phi_\mathbf{l}^1(\mathbf{x}) + \sum_{j=1}^{J-1}\sum_{\mu=1}^{2n-1}\sum_{\mathbf{k}\in\mathcal{K}^{\mu,j}} d_\mathbf{k}^{\mu,j}\psi_\mathbf{k}^{\mu,j}(\mathbf{x}), \tag{13}$$

where n denotes the number of spatial dimensions, bold subscripts denote n-dimensional indices, while $\mathcal{L}^1$ and $\mathcal{K}^{\mu,j}$ are n-dimensional index sets associated with scaling functions $\phi_\mathbf{l}^1$ and wavelets $\psi_\mathbf{k}^{\mu,j}$, respectively. Each of the basis functions, *i.e.* $\phi_\mathbf{l}^1$ or $\psi_\mathbf{k}^{\mu,j}$, corresponds one-to-one with a grid point $\mathbf{l} \in \mathcal{L}^1$ or $\mathbf{k} \in \mathcal{K}^{\mu,j}$. Scaling functions $\phi_\mathbf{l}^1$ carry the averaged signal, while the multi-dimensional second-generation wavelet functions $\psi_\mathbf{k}^{\mu,j}$ define local, variational details. The amplitudes are given by the coefficients $c_\mathbf{l}^1$ and $d_\mathbf{k}^{\mu,j}$, respectively, and hence have a unique correspondence to grid points. Levels of resolution span over $1 \leqslant j \leqslant J$, with J being the maximum level present in the approximation (associated to the finest grid resolution). During wavelet transform, detail (or wavelet) coefficients $d_\mathbf{k}^{\mu,j}$ are obtained recursively from scaling coefficients $c_\mathbf{k}^{\mu,j}$ from level

$J-1$ to 1. After wavelet transform, grid points $\mathbf{l} \in \mathcal{L}^1$ at the coarsest level store the scaling coefficients $c^1_{\mathbf{l}}$, and all the other grid points $\mathbf{k} \in \mathcal{K}^{\mu,j}$ at higher levels store the wavelet coefficients $d^{\mu,j}_{\mathbf{k}}$. To avoid ambiguity, grid points $\mathbf{k} \in \mathcal{K}^{\mu,j}$ with $1 \leqslant j \leqslant J-1$ represent all collocation points located at level $2 \leqslant j \leqslant J$. Note that for n-dimensional space, there are $2n-1$ families of wavelet functions, μ.

Wavelet threshold filtering arises naturally from the series expansion (13). The filtering operation is performed by applying the wavelet transform to the original field $u(\mathbf{x})$, zeroing the wavelet coefficients below a given threshold, $\epsilon = \epsilon(\mathbf{x}, t)$ for generality, and transforming back to the physical space. The resulting approximate field, say $u^{>\epsilon}(\mathbf{x})$, composed of a subset of the original wavelets, represents the dominant modes and formally can be written as the conditional series

$$u^{>\epsilon}(\mathbf{x}) = \sum_{\mathbf{l}\in\mathcal{L}^1} c^1_{\mathbf{l}}\phi^1_{\mathbf{l}}(\mathbf{x}) + \sum_{j=1}^{J-1}\sum_{\mu=1}^{2n-1} \sum_{\substack{\mathbf{k}\in\mathcal{K}^{\mu,j} \\ |d^{\mu,j}_{\mathbf{k}}|>\epsilon\|u(\mathbf{x})\|}} d^{\mu,j}_{\mathbf{k}}\psi^{\mu,j}_{\mathbf{k}}(\mathbf{x}). \tag{14}$$

In many implementations, the filter threshold is taken to be relative to some characteristic scale, often represented by either the L_2- or $L_\infty-$ norm of $u(\mathbf{x})$ and denoted as $\|u(\mathbf{x})\|$.[7] The resulting nonlinear filtering operation separates resolved flow structures and unresolved residual motions. For a properly normalized threshold, the reconstruction error of the filtered variable is shown to converge as[25]

$$\|u^{>\epsilon} - u\| \leqslant O(\epsilon)\|u\|. \tag{15}$$

The dynamic grid adaptation is tightly coupled with the wavelet filter. Due to the one-to-one correspondence between wavelets and grid points, the latter are omitted from the computational mesh if the associated wavelets are omitted from the representation (14). The multilevel structure of this wavelet approximation provides a natural way to obtain the solution on a near optimal numerical grid, which is dynamically adapted to the evolution of the main flow structures, both in location and scale, while higher resolution computations are carried out where (and only where) steep gradients in the resolved flow field occur.

The multi-resolution wavelet decomposition (14) is used for both grid adaptation and interpolation, while a hierarchical finite difference scheme, which takes advantage of the wavelet interpolating properties, is used to differentiate the local function approximations, and to provide the values of derivatives of the function at those particular locations.

III.B. Adaptive-Anisotropic Wavelet Collocation Method

Second-generation wavelet bases described in section III.A rely on topologically rectilinear grids and inherently isotropic mesh elements, which, despite being a highly valuable methodology for the numerical solution of fluid dynamics equations due to mathematical rigor, simplicity and computational efficiency,[26] puts some limitations on the applicability of the approach. These limitations were recently overcome with the development of the Adaptive-Anisotropic Wavelet Collocation Method (A-AWCM).[18] A-AWCM preserves active error-controlling properties of the original AWCM, but provides additional flexibility to control mesh anisotropy and to solve the problem in complex domains by separating the computational space from the physical one and introducing a mapping between them, thus, allowing the use of anisotropic curvilinear meshes in complex geometries.

The introduction of a function that maps the physical domain, say $\mathbf{x} \in \Omega_p$, to the computational domain, say $\boldsymbol{\xi} \in \Omega_c$, provides the necessary flexibility of the mesh geometry when dealing with wall-bounded flows, such as channel flows and flows around obstacles. In physical space, a more optimal spatial distribution of mesh points can be realized, where mesh element aspect ratios, grid stretching and orientation of the cells can be properly varied. Furthermore, body-fitted meshes can be constructed with the accurate resolution of the boundary layer and wake regions. At the same time, the structured rectilinear assembly of collocation points in the computational space is retained, which allows one to use computationally efficient discrete wavelet transform and derivative approximations.

A-AWCM utilizes a general curvilinear coordinate mapping function $\mathbf{x}(\boldsymbol{\xi})$, which can be either continuous or discrete. The mapping coordinates are viewed as additional variables, which can be adapted on and which can be differentiated in computational space, thus, allowing the construction of the Jacobian matrix

$$\mathcal{J}_{ij} \equiv \frac{\partial x_i}{\partial \xi_j}. \tag{16}$$

Spatial derivatives in physical space are evaluated numerically as

$$\frac{\partial}{\partial x_i} = \frac{\partial \xi_j}{\partial x_i}\frac{\partial}{\partial \xi_j} = \mathcal{J}_{ij}^{-1}\frac{\partial}{\partial \xi_j}, \tag{17}$$

where $\mathcal{J}_{ij}^{-1}$ is the inverse Jacobian matrix. Based on the particular flow structures and flow geometry, mesh anisotropy should be controlled through mapping function or mesh generation, and ideally should take into consideration local flow anisotropy. For instance, more isotropic cells are needed around boundary layer separation points to properly resolve flow physics, while anisotropic meshes should be used in boundary and shear layers. At the same time, additional measures should be taken to avoid the generation of mapping resulting in cells with high skewness, degenerate Jacobian ($\det(\mathcal{J}) \to 0$), or non-smooth mesh lines, since the degradation of the mesh quality can not be fully rectified by the automated mesh refinement. It should be noted that an additional adaptation on physical coordinates can only assure the accuracy of the representation of the physical coordinates and would result in additional mesh refinement in the regions where the mesh is ill-conditioned, but does not guarantee the optimality of the mesh anisotropy, which could be controlled only as a part of mesh generation process.

III.C. A-AWCM with Periodic Boundary Conditions

Special consideration should be given to the case when physical domain has periodic boundary condition, since physical coordinates are not periodic. In this case the mesh adaptation can be performed on the coordinate perturbations x_i^{prd} defined by

$$x_i^{\mathrm{prd}} = x_i - \mathcal{J}_{ip}^{\mathrm{prd}}(\xi_p - \min(\xi_p)), \tag{18}$$

where $i = 1, \ldots, n$, repeated index p assumes summation only along periodic directions, and $\mathcal{J}_{ip}^{\mathrm{prd}}$ is the linear with respect to ξ_p Jacobian, given by

$$\mathcal{J}_{ip}^{\mathrm{prd}} = (\, x_i|_{\xi_p=\max(\xi_p)} - x_i|_{\xi_p=\min(\xi_p)})/(\max(\xi_p) - \min(\xi_p)). \tag{19}$$

Note that for simply translated periodic boundaries x_i^{prd} is constant. Rewriting Eq. (18) for x_i and substituting into Eq. (16) results in the following Jacobian matrix

$$\mathcal{J}_{ij} = \frac{\partial x_i^{\mathrm{prd}}}{\partial \xi_j} + \mathcal{J}_{ip}^{\mathrm{prd}}\delta_{pj} + \frac{\partial \mathcal{J}_{ip}^{\mathrm{prd}}}{\partial \xi_j}(\xi_p - \min(\xi_p)), \tag{20}$$

where index p assumes summation only in periodic directions. Note that the linear Jacobian (19) is not a function of ξ_p, resulting in $\dfrac{\partial \mathcal{J}_{ip}^{\mathrm{prd}}}{\partial \xi_j} = 0$ if $j = p$, while the term $\mathcal{J}_{ij}^{\mathrm{prd}} = 0$ when j is the non-periodic direction.

IV. Simulations and Results

IV.A. Supersonic channel flows

In this subsection, simulations of supersonic channel flows are presented for verification of the W-URANS turbulence modeling approach. The simulations are carried out using a fourth-order A-AWCM described in Section III. The grid adaptation is performed on momentum, total energy and temperature fields scaled by L_2 norm with wavelet filtering threshold $\epsilon = 1 \times 10^{-3}$. Relatively small ϵ should be used for W-URANS, since the unknown variables in the RANS equations are mean Reynolds-averaged or Favre-averaged quantities and the threshold ϵ controls the error of solutions (cf. Eq. (15)). All numerical configurations described in this paragraph hold in the remaining context.

The computational domain size is $4\pi H \times 2H \times 4\pi H/3$ in steam-wise(x), wall-normal(y) and span-wise(z) directions, respectively, where H is the half height of the channel. The bulk Reynolds number is $Re = \rho_b u_b H/\mu_w$, and the Mach number is $Ma = u_b/c_w$, where $(\cdot)_b$ and $(\cdot)_w$, respectively, denote bulk mean quantities and quantities averaged at the walls, and c is the speed of sound. The friction Reynolds number $Re_\tau = \rho_w u_\tau H/\mu_w$ where $u_\tau = \sqrt{\tau_w/\rho_w}$. Here, τ_w indicates the wall shear stress. Two different flow configurations are considered: $Re = 3000$ with $Ma = 1.5$ (CH1) and $Re = 6000$ with $Ma = 3.0$ (CH2).

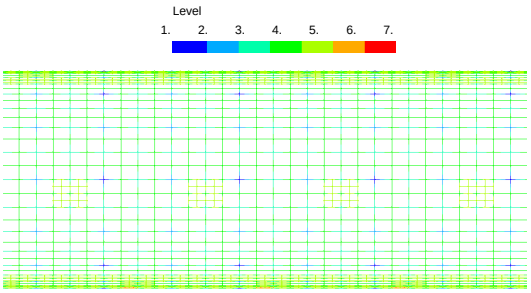

(a) A section of adaptive grids of CH1-2DF colored by levels of resolution.

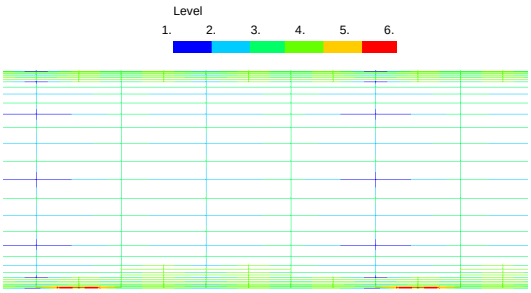

(b) A section of adaptive grids of CH1-2DC colored by levels of resolution.

Figure 1. Adaptive grids retained after converging.

A feedback control of the body force in the stream-wise direction based on the bulk mass flow rate is employed to maintain the desired flow rate. Initial conditions are as follows: the laminar parabolic velocity profile for plane Poiseuille's channel flows, uniform density and total energy. Initial conditions for k, ω or $\tilde{\nu}$ have correspondingly prescribed values at the wall and exponentially approach to uniform values in the free stream.

Two-dimensional channel flow with $Re = 3000$ and $Ma = 1.5$ is used for verification of RANS implementations. The discretization of the computational domain is done by using dyadic nested wavelet collocation grids for the wavelet decomposition (14). Two different computational grids are used. A finer mesh has $J = 7$ and effective resolution 640×256 and a coarser mesh has $J = 6$ and effective resolution 128×192. Using A-AWCM, the mesh is stretched in the wall normal direction following a hyperbolic tangent distribution. The finer mesh case is denoted as CH1-2DF while the coarser mesh case as CH1-2DC. See detailed parameters in Table 1. In the table, $\Delta x^+/\Delta y^+$ is the grid aspect ratio in the immediate vicinity of the wall, while $\Delta y(1)^+$ is the first wall normal grid spacing. Stretching ratio represents the grid spacing expanding rate of successive grids in the y direction, *i.e.* $\Delta y(k)/\Delta y(k-1)$, where k denotes the grid index. Compression ratio is defined as the percentage of collocation points discarded in the adaptive grid compared to the number of non-adaptive grid points.

The S-A model is known to be very robust for aerodynamic flows with high Mach numbers and is therefore examined in this work. For time integration, the explicit standard four-stage Runge-Kutta scheme is applied for the S-A model. The adaptive meshes for case CH1-2DF and CH1-2DC solved with the S-A model are displayed in Figure 1. More grid points are preserved in the near-wall regions whereby the adaptive mesh refinement occurs. However, the meshes in the middle of the channel appear fairly 'non-adaptive', where the RANS solutions are steady and smooth. The actual degrees of freedom are quite reasonable with fairly good compression ratios (see Table 1).

Mean velocity profiles across the channel obtained by the two mesh setups with different aspect ratios are compared with the DNS data[27] and plotted in Figure 2. Both results of distinct meshes agree with DNS quite well. Considering the effect of compressibility, the Van Driest transformed velocity profiles[28] collapse according to Morkovin hypothesis[29] and are compared in Figure 3(a). The mean temperature profiles normalized by the wall averaged temperature are also plotted (Figure 3(b)).

Although the performance of the S-A model is fairly good with the W-URANS method as shown above,

Table 1. Mesh parameters for supersonic channel flows.

Case	Effective resolution	J	$\Delta x^+/\Delta y^+$	$\Delta y(1)^+$	Stretching ratio	Compression ratio
CH1-2DF	640×256	7	17	0.26	1.04	96.5%
CH1-2DC	128×192	6	63	0.34	1.06	95.5%
CH1-3DF	$640 \times 256 \times 320$	7	17	0.26	1.04	99.1%
CH2-2DC	256×192	6	102	0.27	1.06	93.0%

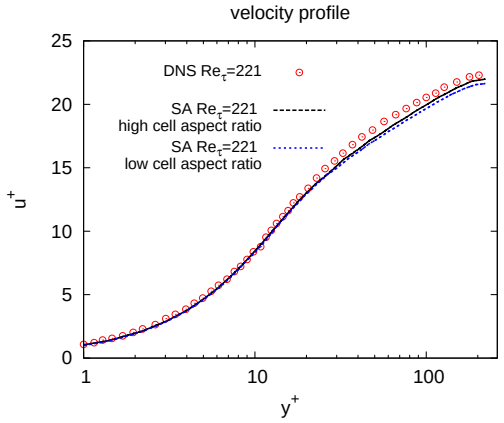

Figure 2. Velocity profiles with different grid aspect ratios solved with the S-A model. DNS data from Ref. 27.

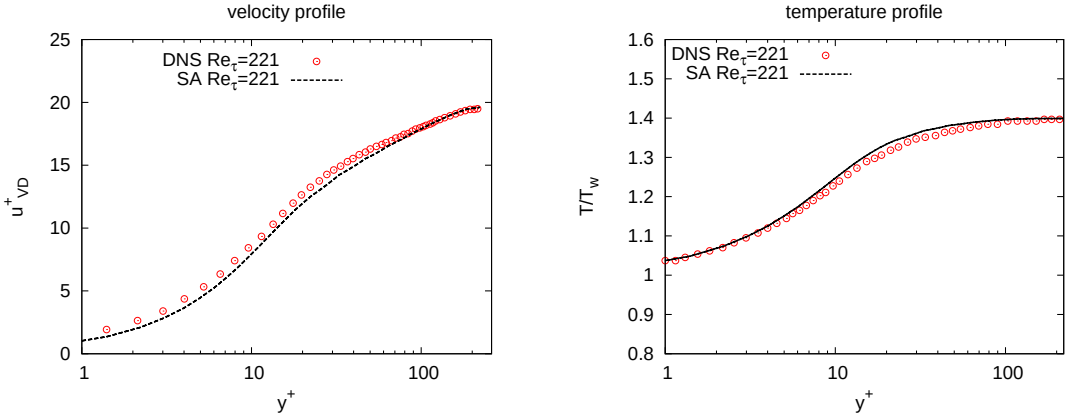

(a) Van Driest transformed velocity profiles. $u^+_{VD} = \int_0^{u^+} (\rho/\rho_w)^{1/2} du^+$. DNS data from Ref. 27.

(b) Temperature profiles. DNS data from Ref. 30.

Figure 3. Velocity and temperature profiles.

the $k-\omega$ model encounters convergence problems due to the singularity of the variable ω at a no-slip wall. Analytically, ω varies like $1/y^2$ as $y \to 0$, while in practice, a large approximate value of ω is specified at the wall, cf. Eq. (10). This approximation for the boundary condition gives rise to serious numerical stiffness, and hence may cause oscillations and convergence problems when it is implemented with high order schemes like the one used in this work. Furthermore, this singular behavior near the wall necessitates the use of implicit time integration schemes. The Crank-Nicolson method is used in this work. Different values of $\omega|_w$ have been tested by increasing δ_h from $\Delta y(1)$ in Eq. (10). It was observed that the simulations blew up unless $\omega|_w$ reduced to the value with $\delta_h > 10\Delta y(1)$, where $10\Delta y(1)$ corresponded to a wall distance with $y^+ \approx 5$. Unfortunately, the solution produced using this $\omega|_w$ substantially overestimated the friction Reynolds number Re_τ by over 10%.

To alleviate this issue, an alternative formulation of the transport equation rewritten for the scalar $\tilde{\omega} = 1/(\omega^{1/2})$, which goes like y as $y \to 0$, is implemented and its robustness and accuracy is improved. First, the explicit time integration scheme can then be used. Then, larger values of $\omega|_w$ can be applied with converged solutions, which produce better results. Figure 4 shows the sensitivity of $\omega|_w$ to the velocity profiles and Re_τ. When the same actual $\omega|_w$ value is applied with the different ω related equations, there is a slight discrepancy. This may be explained that in the implementation of the new $\tilde{\omega}$ equation, a lower bound is used to limit the entire $\tilde{\omega}$ field, which is the actual boundary condition for $\tilde{\omega}|_w = 1/(\omega|_w^{1/2})$. However, no upper bound limiter is used for the original ω field.

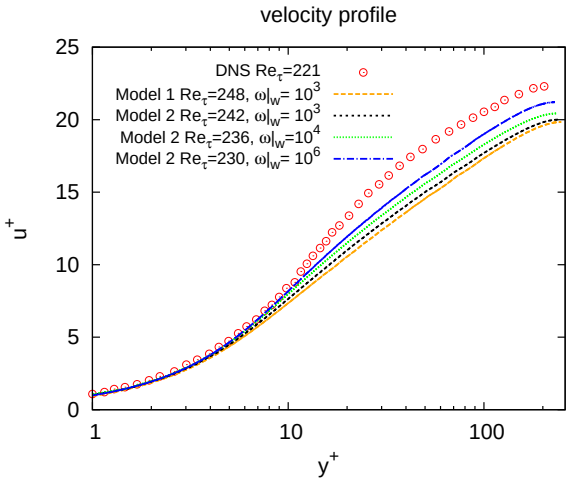

Figure 4. Velocity profiles with different ω wall boundary conditions. Model 1 indicates the original ω equation and Model 2 indicates the equation in terms of $\tilde{\omega} = 1/(\omega^{1/2})$.

The turbulent kinetic energy k and dissipation rate $\varepsilon = \beta^* k\omega$ profiles are depicted in Figure 5. For smaller $\omega|_w$, k is overestimated throughout the wall-normal direction across the channel whereas ε is only significantly overestimated around $y^+ \approx 10$. Overall, the eddy viscosity μ_T is overestimated and thereby higher Re_τ is predicted. Since the poor performance of the $k-\omega$ model for simulations of internal flows, the remaining test cases of internal flows utilize the S-A model only.

To investigate the 3D effect of the channel flow case with the W-URANS method, a 3D simulation with the same Re and Ma is performed with computational grids denoted as CH1-3DF in Table 1. The resulting solution fields resolve fairly week 3D perturbations though the effective grid resolution is considered sufficiently fine. Both the adaptive mesh and results are very similar to the 2D case. This is demonstrated by the velocity profiles from both 2D and 3D simulations shown in Figure 6. These observations may be explained by dissipation nature of the turbulence model so that the 3D W-URANS simulation of this plane channel flow converges to a steady and smooth solution.

A higher Reynolds number $Re = 6000$ and Mach number $Ma = 3.0$ channel flow case is investigated with 2D W-URANS. This case has larger variations of density and thermodynamic changes. The S-A model is tested to capture the Mach number effects. The adaptive mesh parameters are shown in Table 1 referred to as CH2-2DC. Figure 7 plots the mean velocity and wall-average normalized density profiles. The good agreements of the data with the DNS results demonstrate the reliability of the S-A model for simulations of compressible turbulent flows using the W-URANS method.

High levels of grid anisotropy, *i.e.* large grid cell aspect ratios (up to 100) and wall normal stretching ratios work fine for this W-URANS channel flow case, which demonstrates the capability of the A-AWCM methodology. It is legitimate to do so also because there is no flow separation in plane channel cases otherwise separation points would be difficult to resolved by fairly anisotropic grids. A case with flow separation is considered in the next section.

IV.B. A channel flow with periodic hill constrictions

A flow through a channel with periodic hill constrictions is a typical benchmark to investigate the flow physics of turbulent separated flows over smooth surfaces and to validate different RANS and LES solutions with high fidelity DNS and LES data sets. The flow consists in polynomial-shaped obstacles mounted on a flat plate with recirculation region in their wake. It is Case 81 of European Research Community of Flow, Turbulence and Combustion (ERCOFTAC) "Classic Collection" Database. Periodic hill crests are separated by $9H$ and channel height from the plane top wall to the hill feet is $L_y = 3.035H$, where H is the hills' height. For 3D cases, the size of the span is $4.5H$.

A 2D simulation is presented first here with $Re = 2800$ and $Ma = 0.2$. The S-A turbulence model is used. The Reynolds number is based on H and the bulk velocity between the hill crests and the top wall. In actual implementation, a feedback control of the body force in strea-wise (x) direction based on the volume bulk

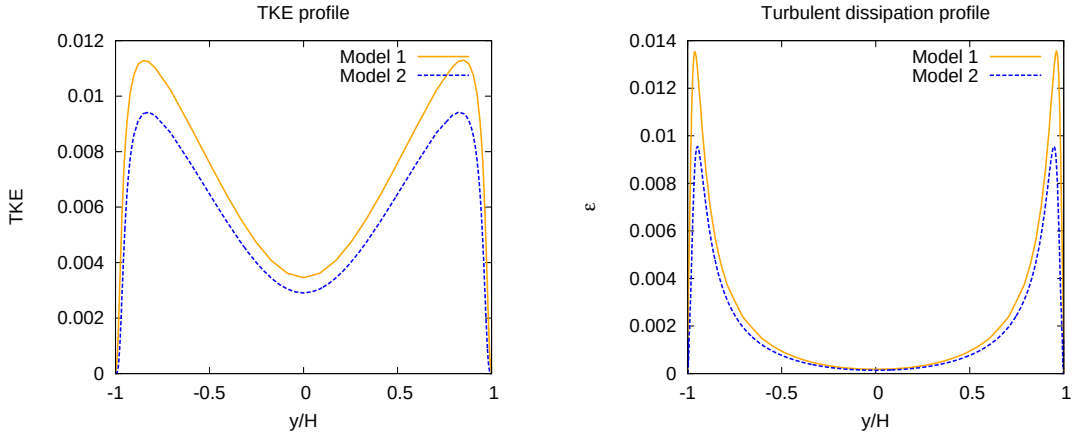

(a) Turbulent kinetic energy profiles.

(b) Turbulent dissipation rate profiles.

Figure 5. Turbulence quantities profiles. Model 1 indicates the original ω equation with $\omega|_w = 10^3$ and Model 2 indicates the equation in terms of $\tilde{\omega} = 1/(\omega^{1/2})$ with $\omega|_w = 10^6$.

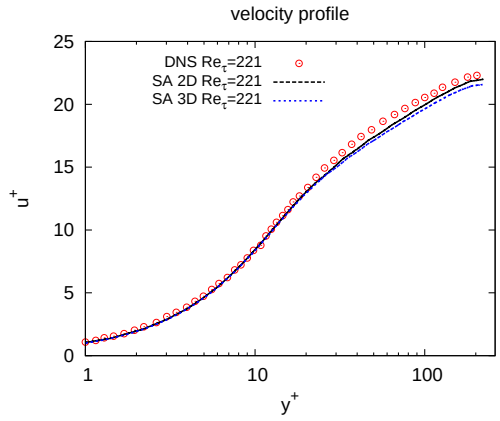

Figure 6. Comparison of velocity profiles by 2D and 3D simulations.

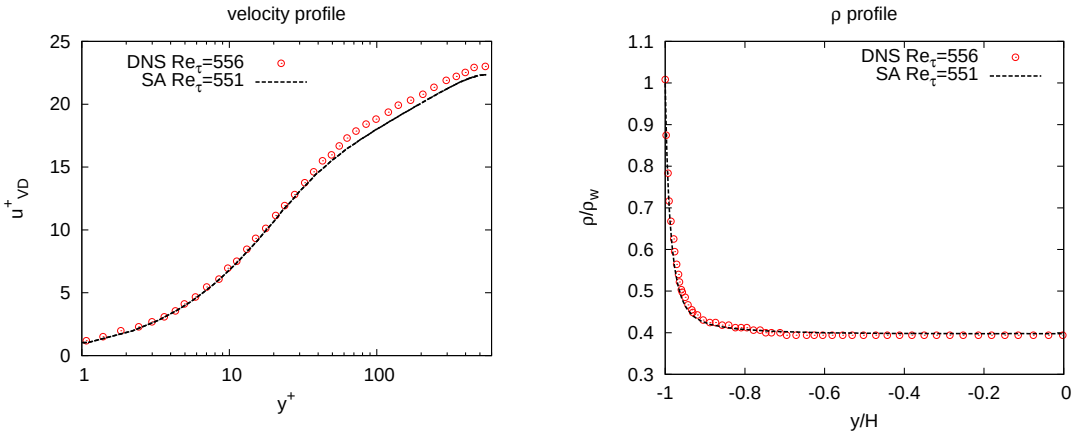

(a) Van Driest transformed velocity profile. $u^+_{VD} = \int_0^{u^+} (\rho/\rho_w)^{1/2} du^+$. DNS data from Ref. 31.

(b) Density profile. DNS data from Ref. 31.

Figure 7. Results of the channel flow case with $Re = 6000$ and $Ma = 3.0$.

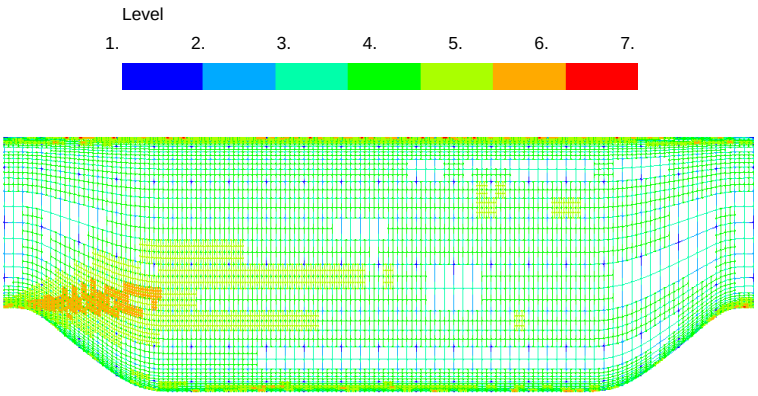

Figure 8. Adaptive grids retained after converging colored with levels of resolution. Local mesh refinement is needed at the separation point.

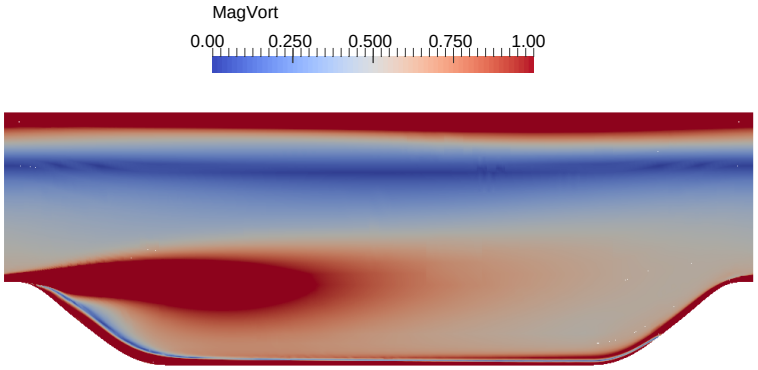

Figure 9. Instantaneous vorticity magnitude contours.

mass flow rate is employed to maintain the desired flow rate. The Reynolds number based on the volume bulk mass flow rate is $Re_v = 0.72Re$.[32] A zero momentum initial condition and uniform density and total energy are specified. In the early stage of the simulation, a relatively large constant body force is used to push the flow until the bulk flow reaches its desired value, after which the feedback mechanism is enabled.

The wavelet collocation grids are comprised of 2560×768 grid points at the finest level $J = 8$. A body-fitted mesh is generated using a two-boundary method with analytical grid coordinates defined between the top and bottom boundaries. Grid points are evenly distributed in the x direction. For grid points along the y direction with the same x coordinate, a hyperbolic distribution is employed to define the y coordinates between the wall boundary nodes. The wall neighboring grid aspect ratio is $\Delta x^+/\Delta y^+ \approx 13$ and $\Delta y^+(1)_{max} \approx 0.11$. The ultimate compression ratio for this case is 99.1% and the corresponding adaptive mesh is depicted in Figure 8. Local mesh refinement occurs around the separation point and upstream part of the separation line as well as the near wall viscous sublayers. The grid cell aspect ratios over the separation bubble region are nearly isotropic so that the separated flow can be resolved and no numerical aliasing and instability occur. Since stream-wise periodicity is specified, the curvilinear Jacobian tensor is modified according to Eq. (20). In addition, the periodic coordinate perturbations x_i^{prd} in Eq. (18) are adapted to resolve the physical coordinates more accurately.

The vorticity magnitude field is displayed in Figure 9, and the mean skin friction coefficient C_f distribution along the bottom wall is plotted and compared with the DNS data[33] in Figure 10. As is expected, this 2D W-URANS simulation cannot predict the size of the separation bubble and reattachment precisely, while the W-RANS predicted C_f over the first hill agrees fairly well with the DNS result.

The corresponding 3D case is also carried out. A periodic boundary condition is imposed for the span-wise direction. The grid resolution in the X-Y plane is the same as the 2D case while the domain size in the

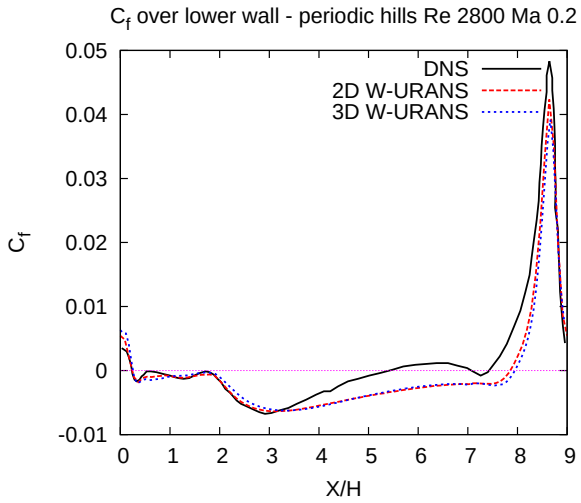

Figure 10. Time-averaged (and span-wise averaged for 3D) skin friction coefficient on the lower wall. DNS data from Ref. 33.

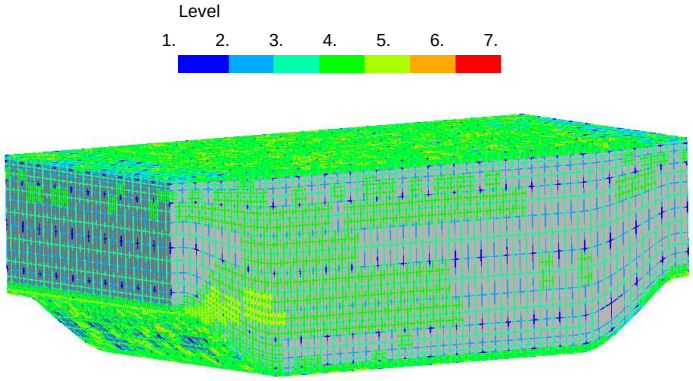

Figure 11. 3D adaptive grids colored with levels of resolution. Local mesh refinement is needed near the wall and at the separation point.

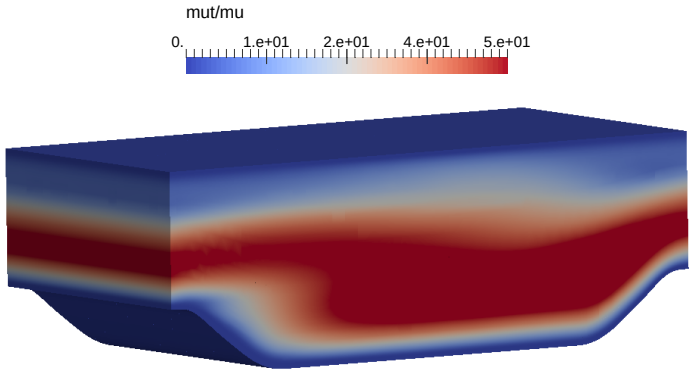

Figure 12. 3D instantaneous μ_T/μ contours.

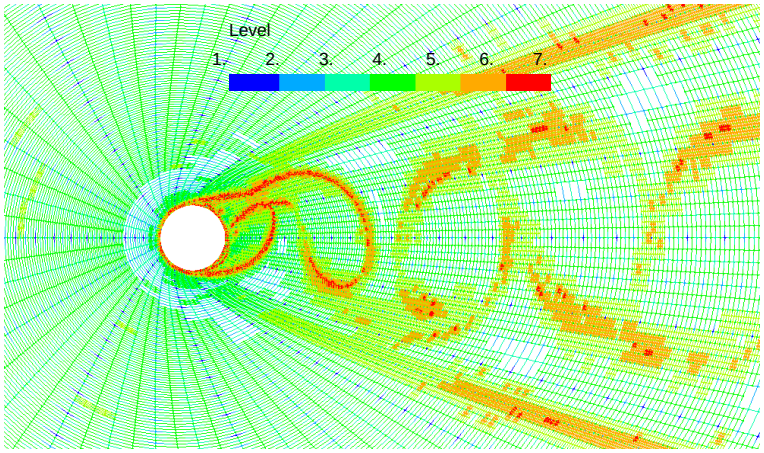

Figure 13. Adaptive grids colored by the levels of resolution for the 2D case.

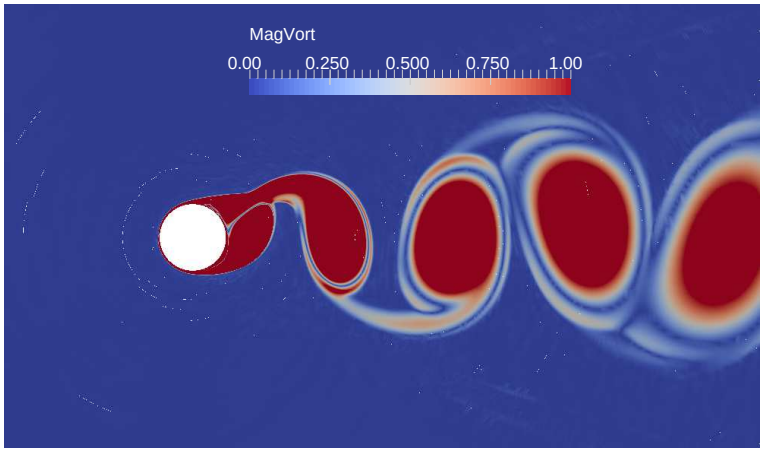

Figure 14. Vorticity magnitude contours for the 2D case.

span-wise direction follows the same value $4.5H$ as in the literature. The number of grid points at the finest level of resolution in the Z direction is 1280 with even distribution. It is shown in Figure 11 and 12 that the eddy viscosity predicted by the S-A model is substantial enough to dissipate small scale flow structures and the flow field is quasi two-dimensional. Therefore the mean skin friction coefficient over the curved lower wall shown in Figure 10 is nearly the same as the 2D case. Meanwhile, the actual number of grid points is about 1.1 million with correspondingly quite significant compression ratio of 99.956% due to the smoothness of Reynolds averaged fields.

IV.C. A flow past a circular cylinder

The simulation setup follows Ref. 19. The flow configuration is a flow past a circular cylinder at a sub-critical Reynolds number $Re = \rho_0 U D/\mu_0 = 3900$ and Mach number $Ma = U/c_0 = 0.2$, where U is the free-stream velocity and $c_0 = \sqrt{\gamma p_0/\rho_0}$ is the ambient speed of sound. The $k-\omega$ model has been examined[19] with the W-URANS method whereas the S-A model is tested in this work and the complete results is compared. An analytically azimuthal and the radial distributions of grid points proposed by Beaudan and Moin,[34] based on the so-called wake envelope, are employed in the physical domain. More efficient resolution of the shedding vortex street and numerical mesh elements with better anisotropy in the boundary layer are obtained in the wake region.

The flow around the two-dimensional cross-section of the cylinder is described in a Cartesian coordinate system (x, y), where the x axis corresponds to the inflow direction. In polar coordinates (r, θ) an annular

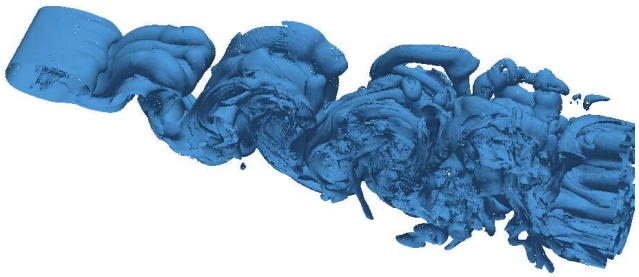

(a) W-URANS using the $k-\omega$ model with model coefficients described in Ref. 19.

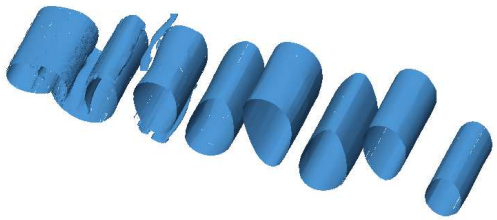

(b) W-URANS using the S-A model described above.

Figure 15. Iso-surfaces of the instantaneous vorticity magnitude field at $0.5U/D$.

physical domain is defined by $0.5 < r/D < 20$ and $0 < \theta < 2\pi$. For the 3D case, span-wise width, which plays an important role for crossflow around a circular cylinder,[35] is prescribed as $0 < z/D < \pi$, following similar computational studies.[36] A convergence test[19] has been performed using different J and wavelet filter threshold ϵ. It shows that $J = 7$ and $\epsilon = 5 \times 10^{-4}$ is sufficient for grid convergence with the base (coarsest level) grids $40 \times 12 \times 2$. For spatial resolution, on the finest grid ($j = J$), the first point is located at a radial distance $r \approx 3 \times 10^{-4} D$ from the surface. Meanwhile, the cells adjacent to the body surface have an aspect ratio of approximately 5:2.

Solutions for a 2D simulation using the the S-A model are depicted in Figure 13 and 14. Figure 13 shows the instantaneous adaptive mesh. The corresponding vorticity magnitude contours are depicted in Figure 14. Note that in this case the grids are adapted on the vorticity magnitude and L_2 norm of the train rate tensor in addition to adaptation on primary variables, *i.e.* momentum and total energy. These adapted quantities are scaled by their L_∞ norms, which follows Ref. 19 and is different from the other cases in this report. Adaptive mesh refinement is observed in Figure 13 to resolve the vorticity field. The active number of grid points for this 2D case with the S-A model is about 160,000 with compression ratio about 92%.

It is observed in Ref. 19 that unlike conventional URANS simulation, the W-URANS in the 3D case using the $k-\omega$ model is able to capture the 3D vortical structures and thereby produce substantial improvement with respect to 2D W-URANS and 3D conventional non-adaptive low-resolution URANS. The S-A model is also examined for the 3D simulation and the results are compared here. From the iso-surfaces of the instantaneous vorticity magnitude plotted in Figure 15, one can easily identify the significant difference between the solutions of the two RANS models. Unlike the $k-\omega$ model, the S-A model produces quasi one-dimensional vortices. Its solution is more similar to a conventional 3D URANS computation. Subsequently, the number of adaptive grid points needed by the S-A model is substantially less than the $k-\omega$ model, reducing from about 30 million to 3 million with compression ratio from 90% to 99%.

This is the consequence of the turbulent eddy viscosity field predicted by the two distinct models shown in Figure 16 and 17. The S-A model turns out to overestimate the eddy viscosity dramatically compared to the $k-\omega$ model. In the $k-\omega$ model, used by Ref. 19, the cross-diffusion term applied on the right hand side of the original ω transport equation has its coefficient $\sigma_{d0} = 0.5$ as used by Kok.[37] This cross-diffusion term is devised to improve results for free-shear layers, *e.g.* the wake flow in this case, when using the $k-\omega$ model. It is an extra source term of the ω equation and hence reduces the net production of the turbulent kinetic energy, which in turn reduces the eddy viscosity in the wake region and then decreases the predicted spreading rates. This may explain the low level of computed eddy viscosity in the wake region by the $k-\omega$ model.

Using diffusion coefficients used by Kok[37] is reported underestimating the spreading rate than measured data for the wake flow.[22] This is reflected by the wake profiles of the velocity components at $X/D = 3$ plotted in Figure 18. The deficit stream-wise velocity predicted by 3D W-URANS with the $k-\omega$ model is much higher than the experimental data and other URANS results, while the corresponding wake width is narrower than the others. On the contrary, 3D W-URANS with the S-A model predicts the closest stream-

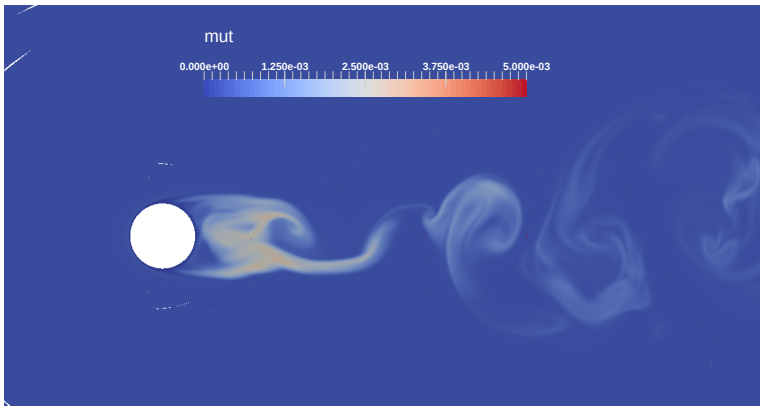

Figure 16. Eddy viscosity contours using the $k-\omega$ model for the 3D case.

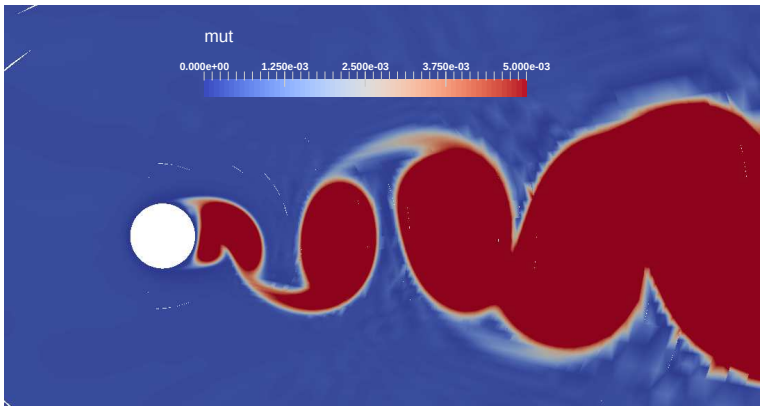

Figure 17. Eddy viscosity contours using the S-A model for the 3D case.

wise velocity profile to the experimental data. For the cross-flow components, the $k-\omega$ model performs the best compared to the conventional 3D URANS and W-URANS with the S-A model. The conventional URANS predicts opposite signs for the cross-flow component, while the W-URANS with the S-A model predicts correct signs but lower magnitudes. All 2D simulations compared in the plots underestimate deficit stream-wise velocity and cross-flow velocity in magnitudes.

The mean pressure coefficient over the surface of the cylinder and steam-wise velocity along the centerline in the near wake region are plotted in Figure 19. It is shown that 2D results are quite similar among different predictions with lower back pressure over the surface and larger stream-wise velocity along the central line in the near wake, compared to the measured data. The 3D W-URANS with the S-A model produces very similar pressure coefficient with the conventional 3D URANS, while the 3D W-URANS with the $k-\omega$ model gives more accurate but slightly overestimated results compared with the experimental data. For the stream-wise velocity distribution, the 3D W-URANS with the $k-\omega$ model performs better in the very near wake $X/D < 1.5$ while the W-URANS with the S-A model matches the data well downstream $X/D = 3.5$ where the other two predictions produce lower values of this velocity component.

The integral quantities of the flow are reported in Table 2 comparing between the current and previous work. The mean drag coefficient $\overline{C_D}$, the mean base pressure coefficient $\overline{C_{P_b}}$, the Strouhal number $St = fD/U$ (with f the vortex shedding frequency), the root-mean-square value of the lift coefficient C_l' and the mean separation angle $\overline{\theta_s}$ are presented. The 2D results are consistently poor compared with the 3D ones. The 3D W-URANS with the $k-\omega$ model appears to underestimate while all the other simulations tend to overestimate all parameters except $\overline{\theta_s}$. For the W-URANS with the S-A model, its 2D and 3D cases produce the closest results compared with the other reference simulations, though its grid spacing of the finest level of resolution is about $0.02D$ - the same as the W-URANS with the $k-\omega$ model. This outcome suggests that the S-A model is fairly more dissipative than the $k-\omega$ model and the quasi one-dimensional vortex structure

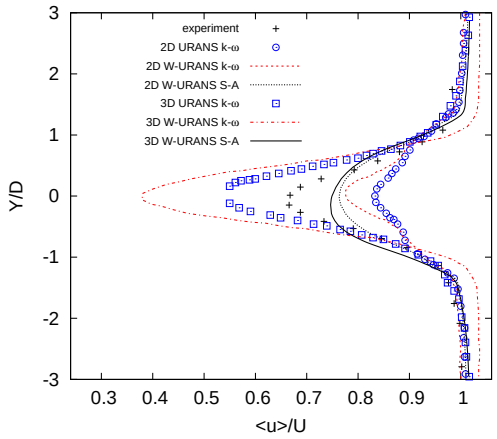

(a) Span-wise and time averaged $\langle u \rangle / U$ in the near wake located at $X/D = 3$.

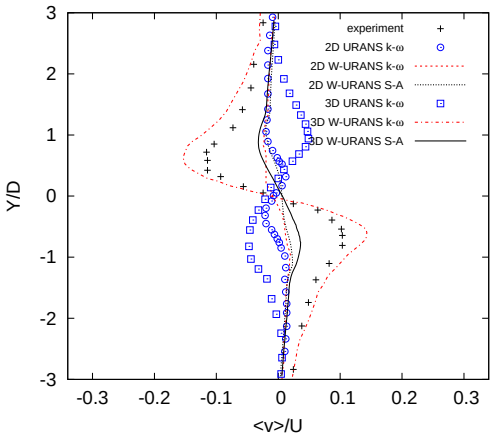

(b) Span-wise and time averaged $\langle v \rangle / U$ in the near wake located at $X/D = 3$.

Figure 18. Mean velocity profiles in the near wake located at $X/D = 3$. The experimental data from Ref. 38, 3D URANS results from Ref. 39 and 3D W-URANS results from Ref. 19.

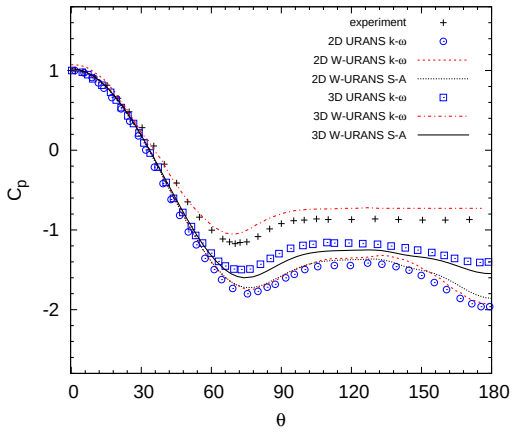

(a) Span-wise and time averaged C_p over the surface.

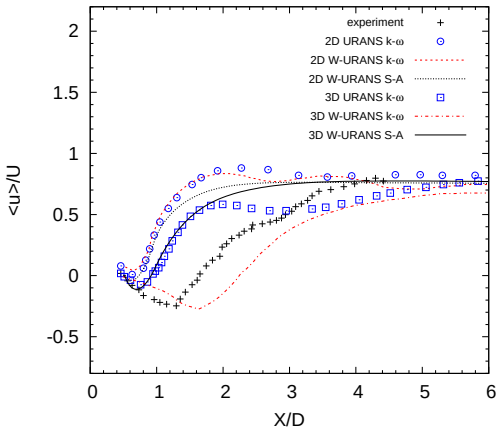

(b) Span-wise and time averaged $\langle u \rangle / U$ along the centerline $Y/D = 0$.

Figure 19. Mean pressure coefficient over the surface of the cylinder and steam-wise velocity along the centerline. The experimental data from Ref. 36, 3D URANS results from Ref. 39 and 3D W-URANS results from Ref. 19.

predicted by the former is determined by the nature of the model regardless the span-wise resolution. Note that the conventional 3D URANS[39] using the $k - \omega$ model chooses a span-wise grid spacing of about $0.2D$. Such *ad hoc* coarse resolution forces its 3D simulation close to the corresponding 2D simulation whereas the W-URANS addresses this issue and guarantees the grid independence by using very fine effective resolution, while keeping the number of computational grid points small.

V. Conclusions

The Wavelet-based Unsteady Reynolds-Averaged Navier-Stokes turbulence modeling approach is developed and validated for simulations of wall-bounded internal and external compressible turbulent flows with the $k - \omega$ and S-A models. The new approach is able to handle arbitrary geometries with body-fitted anisotropic meshes using a curvilinear mapping between the computational and physical domains, while preserving active error-controlling properties of the original adaptive wavelet method. Since a very small adaptive wavelet threshold ($O(10^{-3})$) is applied, the present W-URANS yields nearly identical results as the non-adaptive URANS that uses the same fine grid resolution. This implies grid convergence of the

Table 2. Global flow parameters. Results from W-URANS compared to conventional URANS results and experimental data.

Case	$\overline{C_D}$	$-\overline{C_{P_b}}$	C_l'	St	$\overline{\theta_s}$
2D W-URANS (precent S-A model)	1.55	1.86	1.10	0.227	82
2D W-URANS[19]	1.51	1.95	1.10	0.24	81
2D URANS[39]	1.59	1.96	1.17	0.235	–
3D W-URANS (precent S-A model)	1.50	1.54	1.02	0.220	86
3D W-URANS[19]	0.95	0.74	0.20	0.21	86
3D URANS[39]	1.32	1.42	0.70	0.223	–
experiment[36]	0.99	0.88	–	0.215	86

W-URANS solutions. This is not the case for conventional URANS computations, where very coarse resolution is usually chosen along with numerically dissipative schemes to damp out small turbulent structures. The 3D W-URANS with the S-A model produces results similar to its 2D counterpart, whereas the 3D W-URANS with the $k-\omega$ model is able to resolve small-scale 3D vortical structures. This suggests that the S-A model is intrinsically more dissipative than the $k-\omega$ model though very fine resolution is applied to both models. The current study serves as a baseline for development of a unified hierarchical eddy resolving turbulence modeling framework, capable of performing simulations of different fidelity: from non-modeling direct numerical simulations to full-modeling RANS simulations.

Acknowledgments

This work is supported by NASA's Revolutionary Computational Aerosciences (RCA) discipline under the Transformational Tools and Technologies (TTT) Project Grant No NNX15AU24A. OVV was supported by Russian Science Foundation (Project 16-11-10350). Authors are also thankful for the computing time on NSF XSEDE Stempede and Comet systems and RCC HPC system at Florida State University.

References

[1]Vasilyev, O. V. and Bowman, C., "Second-generation wavelet collocation method for the solution of partial differential equations," *Journal of Computational Physics*, Vol. 165, No. 2, 2000, pp. 660–693.

[2]Vasilyev, O. V., "Solving multi-dimensional evolution problems with localized structures using second generation wavelets," *International Journal of Computational Fluid Dynamics*, Vol. 17, No. 2, 2003, pp. 151–168.

[3]Vasilyev, O. V. and Kevlahan, N. K.-R., "An adaptive multilevel wavelet collocation method for elliptic problems," *Journal of Computational Physics*, Vol. 206, No. 2, 2005, pp. 412–431.

[4]Souopgui, I., Wieland, S. A., Hussaini, M. Y., and Vasilyev, O. V., "Space–time adaptive approach to variational data assimilation using wavelets," *Journal of Computational Physics*, Vol. 306, 2016, pp. 253–268.

[5]Nejadmalayeri, A., Vezolainen, A., Brown-Dymkoski, E., and Vasilyev, O. V., "Parallel adaptive wavelet collocation method for PDEs," *Journal of Computational Physics*, Vol. 298, 2015, pp. 237–253.

[6]Farge, M., Schneider, K., Pellegrino, G., Wray, A. A., and Rogallo, R. S., "Coherent vortex extraction in three-dimensional homogeneous turbulence: Comparison between CVS-wavelet and POD-Fourier decompositions," *Physics of Fluids (1994-present)*, Vol. 15, No. 10, 2003, pp. 2886–2896.

[7]Goldstein, D. E. and Vasilyev, O. V., "Stochastic coherent adaptive large eddy simulation method," *Physics of Fluids*, Vol. 16, No. 7, 2004, pp. 2497–2513.

[8]Goldstein, D. A., Vasilyev, O. V., and Kevlahan, N.-R., "Feasibility Study of an Adaptive Large Eddy Simulation Method," *AIAA Paper*, 2003, pp. 2003–3551.

[9]Goldstein, D. E., Vasilyev, O. V., and Kevlahan, N. K.-R., "CVS and SCALES simulation of 3-D isotropic turbulence," *Journal of Turbulence*, Vol. 6, No. 37, 2005, pp. 1–20.

[10]Kevlahan, N. K. and Vasilyev, O. V., "An adaptive wavelet collocation method for fluid-structure interaction at high Reynolds numbers," *SIAM Journal on Scientific Computing*, Vol. 26, No. 6, 2005, pp. 1894–1915.

[11]Kevlahan, N.-R., Vasilyev, O., Goldstein, D., and Jay, A., "A three-dimensional adaptive wavelet method for fluid-structure interaction," *Direct and Large-Eddy Simulation V*, Springer, 2004, pp. 147–154.

[12]Vasilyev, O. and Kevlahan, N.-R., "Hybrid wavelet collocation–Brinkman penalization method for complex geometry flows," *International journal for numerical methods in fluids*, Vol. 40, No. 3-4, 2002, pp. 531–538.

[13]De Stefano, G. and Vasilyev, O. V., "A fully adaptive wavelet-based approach to homogeneous turbulence simulation," *Journal of Fluid Mechanics*, Vol. 695, 2012, pp. 149–172.

[14]Nejadmalayeri, A., Vezolainen, A., De Stefano, G., and Vasilyev, O. V., "Fully adaptive turbulence simulations based on Lagrangian spatio-temporally varying wavelet thresholding," *Journal of Fluid Mechanics*, Vol. 749, 2014, pp. 794–817.

[15]De Stefano, G., Nejadmalayeri, A., and Vasilyev, O. V., "Wall-resolved wavelet-based adaptive large-eddy simulation of bluff-body flows with variable thresholding," *Journal of Fluid Mechanics*, Vol. 788, 2016, pp. 303–336.

[16]Liu, Q. and Vasilyev, O. V., "A Brinkman penalization method for compressible flows in complex geometries," *Journal of Computational Physics*, Vol. 227, No. 2, 2007, pp. 946–966.

[17]De Stefano, G. and Vasilyev, O. V., "Wavelet-based adaptive simulations of three-dimensional flow past a square cylinder," *Journal of Fluid Mechanics*, Vol. 748, 2014, pp. 433–456.

[18]Brown-Dymkoski, E. and Vasilyev, O. V., "Adaptive-Anisotropic Wavelet Collocation Method on general curvilinear coordinate systems," *Journal of Computational Physics*, 2017.

[19]De Stefano, G., Brown-Dymkoski, E., and Vasilyev, O. V., "Wavelet-based adaptive unsteady Reynolds-averaged turbulence modeling of external flows," To appear in *Journal of Fluid Mechanics*, 2018.

[20]Wilcox, D. C. et al., *Turbulence modeling for CFD*, Vol. 2, DCW industries La Canada, CA, 1998.

[21]Durbin, P. A. and Reif, B. P., *Statistical theory and modeling for turbulent flows*, John Wiley & Sons, 2011.

[22]Wilcox, D. C., "Formulation of the kw turbulence model revisited," *AIAA journal*, Vol. 46, No. 11, 2008, pp. 2823–2838.

[23]Spalart, P. and Allmaras, S., "A one-equation turbulence model for aerodynamic flows," *30th aerospace sciences meeting and exhibit*, 1992, p. 439.

[24]Bardina, J., Huang, P., Coakley, T., Bardina, J., Huang, P., and Coakley, T., "Turbulence modeling validation," *28th Fluid dynamics conference*, 1997, p. 2121.

[25]Donoho, D. L., "Interpolating Wavelet Transforms," Tech. Rep. 408, Department of Statistics, Stanford University, 1992.

[26]Schneider, K. and Vasilyev, O. V., "Wavelet methods in computational fluid dynamics," *Annual Review of Fluid Mechanics*, Vol. 42, 2010, pp. 473–503.

[27]Coleman, G. N., Kim, J., and Moser, R., "A numerical study of turbulent supersonic isothermal-wall channel flow," *Journal of Fluid Mechanics*, Vol. 305, 1995, pp. 159–183.

[28]Van Driest, E. R., "Turbulent boundary layer in compressible fluids," *Journal of the Aeronautical Sciences*, Vol. 18, 1951, pp. 145–160.

[29]Morkovin, M. V., "Effects of compressibility on turbulent flows," *In mécanique de la Turbulence (ed. A. Favre)*, 1962, pp. 367–380.

[30]Morinishi, Y., Tamano, S., and Nakabayashi, K., "Direct numerical simulation of compressible turbulent channel flow between adiabatic and isothermal walls," *Journal of Fluid Mechanics*, Vol. 502, 2004, pp. 273–308.

[31]Foysi, H., Sarkar, S., and Friedrich, R., "Compressibility effects and turbulence scalings in supersonic channel flow," *Journal of Fluid Mechanics*, Vol. 509, 2004, pp. 207–216.

[32]Ziefle, J., Stolz, S., and Kleiser, L., "Large-eddy simulation of separated flow in a channel with streamwise-periodic constrictions," *AIAA journal*, Vol. 46, No. 7, 2008, pp. 1705–1718.

[33]Balakumar, P., "DNS/LES Simulations of Separated Flows at High Reynolds Numbers," *49th AIAA Fluid Dynamics Conference*, 2015, p. 2783.

[34]Beaudan, P. and Moin, P., "Numerical experiments on the flow past a circular cylinder at sub-critical Reynolds number," Tech. rep., DTIC Document, 1994.

[35]Norberg, C., "An experimental investigation of the flow around a circular cylinder: influence of aspect ratio," *Journal of Fluid Mechanics*, Vol. 258, 1994, pp. 287–316.

[36]Kravchenko, A. G. and Moin, P., "Numerical studies of flow over a circular cylinder at Re D= 3900," *Physics of fluids*, Vol. 12, No. 2, 2000, pp. 403–417.

[37]Kok, J. C., "Resolving the dependence on freestream values for the k-turbulence model," *AIAA J*, Vol. 38, No. 7, 2000, pp. 1292–1295.

[38]Ong, L. and Wallace, J., "The velocity field of the turbulent very near wake of a circular cylinder," *Experiments in fluids*, Vol. 20, No. 6, 1996, pp. 441–453.

[39]Young, M. and Ooi, A., "Comparative Assessment of LES and URANS for Flow Over a Cylinder at a Reynolds Number of 3900," *16th Australasian Fluid Mechanics Conference (AFMC)*, School of Engineering, The University of Queensland, 2007, pp. 1063–1070.